

Counting-based particle flux estimation for traffic analysis in live cell imaging

Thierry Pécot, Charles Kervrann, Jean Salamero, Jérôme Boulanger

Abstract—A quantitative analysis of the dynamic contents in fluorescence time-lapse microscopy is crucial to decipher the molecular mechanisms involved in cell functions. In this paper, we propose an original traffic analysis approach based on the counting of particles from frame to frame. The suggested method lies between individual object tracking and dense motion estimation (*i.e.*, optical flow). Instead of tracking each moving particle, we estimate fluxes of particles between predefined and adjacent regions. The problem is formulated as the minimization of a global cost function and the approach allows us to process image sequences with a high number of particles and a high rate of particle appearances and disappearances. We propose to study the influence of object density, image partition scale, motion amplitude and particle appearances/disappearances in a large variety of simulations. The potential of the method is finally demonstrated on real image sequences showing GFP-tagged Rab6 trafficking in confocal microscopy.

Index Terms—intracellular trafficking, particle counting, motion analysis, graphical models, energy minimization, video-microscopy.

I. INTRODUCTION

Fluorescence microscopy enables localizing the distribution of fluorescently tagged proteins of interest along time. The automated quantification of the dynamic behavior of tagged proteins is of major importance in cell biology since it offers a better understanding of fundamental mechanisms including membrane transport, cell signaling, cell division and motility. Here, we focus on traffic estimation [1]–[3] (see Fig. 1) to quantify the interactions between different membrane domains. The monitoring of fluxes between different cell compartments highlights intracellular communication. Moreover, the determination of the number of objects interacting with a region of interest over a given period of time can allow the identification of a potential trigger effect.

In this paper, we propose to estimate the flux of particles and fluorescence intensities between adjacent regions, given a partition of the image. It is worth noting that the fluorescence intensities are proportional to the amount of tagged proteins. Our three-step *counting-based* approach is as follows:

- i) The cell is uniformly partitioned into fixed-size and fixed-shape regions.
- ii) The moving particles are automatically detected using an appropriate algorithm.
- iii) The fluxes are estimated with sparse constraints from an image pair at each time step from temporal variations of

Thierry Pécot and Charles Kervrann are with Inria, Centre Rennes – Bretagne Atlantique, Campus de Beaulieu, 263 Avenue Général Leclerc, 35042 Rennes Cedex, France. Jean Salamero and Jérôme Boulanger are with UMR 144 CNRS / Institut Curie, 12 rue Lhomond, 75005 Paris, France

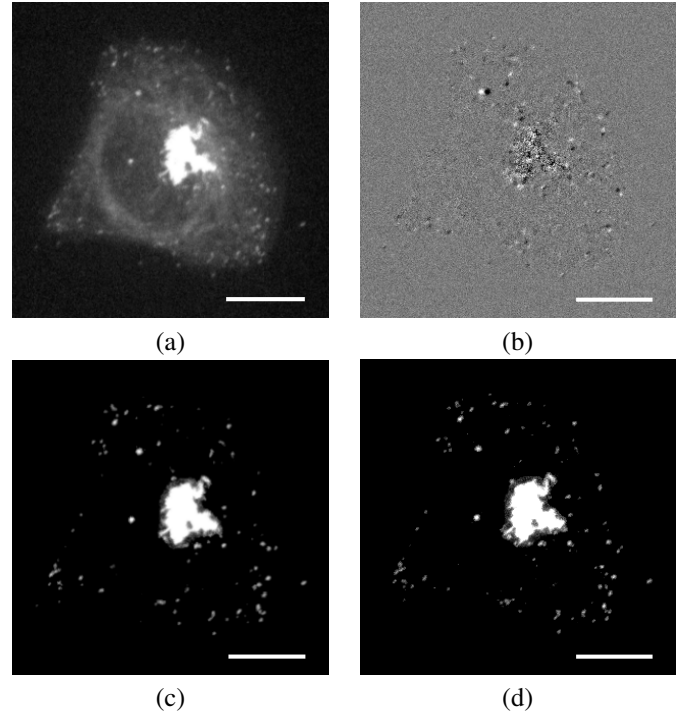


Fig. 1. (a) Maximum projection along the z-axis of a fluorescent image of a sequence showing Rab6-proteins in a crossbow-shaped cell; (b) intensity difference between a pair of images (first image (a)) projected along the z-axis; (c-d) display of moving vesicles in the image pair using the C-CRAFT algorithm [3]. The scale bars correspond to 5 μm .

the number of particles in each region of the uniform tessellation. Except for some trivial cases, the flux estimation is actually an ill-posed problem and additional constraints are necessary to find the optimal solution.

In this modeling, appearances and disappearances can be taken into account by adding a virtual region to the image partition. In real 2D and 3D image sequences, the spots typically appear and disappear because of molecular interactions, photo-bleaching, a low signal-to-noise ratio, limited fields of view or out-of-focus displacement. A preliminary version of the proposed approach was described in [4]. In this paper, we provide the following improvements:

- extension of the method to process 2D and 3D data with the same framework;
- extension of the method to estimate particle and intensity fluxes;
- evaluation of the influence of the sparsity parameter and discussion on the settings of the parameters;
- evaluation on a large set of artificial image sequences;

- application to Rab6 vesicular trafficking;
- comparison with optical flow and particle tracking frameworks.

Related work

The approach we propose can be related to the network tomography originally developed for Internet traffic estimation [5] and applied later to computer vision [6]. In this approach, knowing the routing matrix, the average traffic over time between any region pair in an image partition is recovered from the local traffic measured between adjacent regions; it is not necessary to track an object in an image sequence, but just to determine when an object reaches a region. However, as shown in [7], this computational approach is limited when the number of regions is high in fluorescence video-microscopy. A cell counting approach without cell tracking based on the sum of in-flux and out-flux rates was recently proposed in [8]. Unfortunately, this method cannot be applied to estimate particle fluxes since appearances and disappearances are not taken into account.

Traditionally, particle tracking methods estimate the particle trajectories over time. Therefore, particle fluxes could be obtained from the tracks by identifying the particles crossing the uniform tessellation boundaries from frame to frame. In what follows, we focus on tracking methods that could be applied for flux estimation. Multi-object tracking methods generally involve a frame by frame object detection [9] and an association step across time [10], [11]. While several authors directly address the latter as a distance-based optimization problem [12], this approach generally fails when the density of objects increases or when the localization of the particles is corrupted by noise and clutter. The use of state estimation via for example Kalman filtering has been successfully explored for multi-target tracking [13], [14]. Unfortunately, the performance of these methods decreases when the number of objects increases. Hybrid approaches [15], [16] first connect detected points into short tracks and then link the resulting tracklets together to obtain the final trajectories. These methods are efficient but rely on *ad hoc* mathematical formulations which do not insure the convergence to a global optimum. Particle filtering methods [17] provide an interesting framework to address multi-object tracking. The filter performs both localization and position estimation over time, not only improving temporal matching, but also improving detection accuracy. These sampling-based methods regrettably require a high computational cost and the tuning of several meta parameters. Recently, multiple hypotheses tracking methods have become popular [18], [19]. These methods rely on different global optimization methods, such as linear programming [18] or integer programming [19]. To limit the exponential increase of the solution space, these methods use a sliding time window, leading to sub-optimal solutions. Moreover, these methods rely on a large set of parameters that can be automatically estimated from annotated data, if available. Finally, closer to the approach presented in this paper, a graphical approach investigated in computer vision considers object fluxes between predefined regions to recover the individual object tracks along time [20].

This method is attractive but cannot be directly applied to fluorescence microscopy images because of the high number of particles to track and the possibility for the objects to appear and disappear anywhere in the image, given that these events occur at specified entrances and exits in the observed scene.

The estimation of a dense displacement field may unravel the mechanical constraints taking place in the cell and represents an alternative to tackle the analysis of movement in fluorescence microscopy. The displacement field estimated at several resolution levels could be related to particle fluxes since motion estimation is performed on uniform tessellations. Dominant or average motion vectors in blocks could also be interpreted as intensity fluxes. Generally, block matching techniques based on correlation measures are used in practice to model physical phenomena and typical intensity changes [21], [22]. The temporal stationarity of motion also improves the matching [21], [23]. However, these correlation-based methods remain unable to produce a reliable estimate in arbitrary context because of mismatches due to local correspondence ambiguities and limitations related to locally constant motion assumption. As an alternative, assuming intensity preservation in time, one can derive the optical flow constraint. In this context, two main strategies can be distinguished:

- *Local* approaches are based on the seminal work of Lucas & Kanade [24] and have been applied to several biological problems [25], [26]. The idea is to assume a parametric motion model in a fixed-size neighborhood of each pixel, and to estimate the corresponding parameters by solving the linear system composed of brightness constancy equations at each pixel. It leads to failures in the case of a local lack of intensity gradient or in presence of motion discontinuities.
- *Global* approaches have only recently been investigated for biological purposes [27]–[29]. The idea is to impose smoothness of the flow field via a global regularization model penalizing large spatial variations of the flow field. Associated to variational optimization schemes, global energy models constitute the standard framework of state-of-the-art methods in computer vision benchmarks. However, we observe serious limitations in fluorescence imaging: (i) the use of a coarse-to-fine decomposition to cope with large displacements leads to the loss of small moving structures; (ii) variational optimization tends to over-smooth the motion field; (iii) semi-local intensity changes cannot be easily estimated.

Our approach is a global approach able to process 2D and 3D data but we do not impose a regularized solution as considered in motion estimation methods.

Organization

The remainder of the paper is organized as follows. In Section II, we present the graph-based modeling for flux estimation and describe the sparsity-based cost functional and the optimization method. In Section III, we evaluate the influence of the grid size, the object density, the motion amplitude and the particle appearance and disappearance rate. We also quantitatively compare the proposed method to a

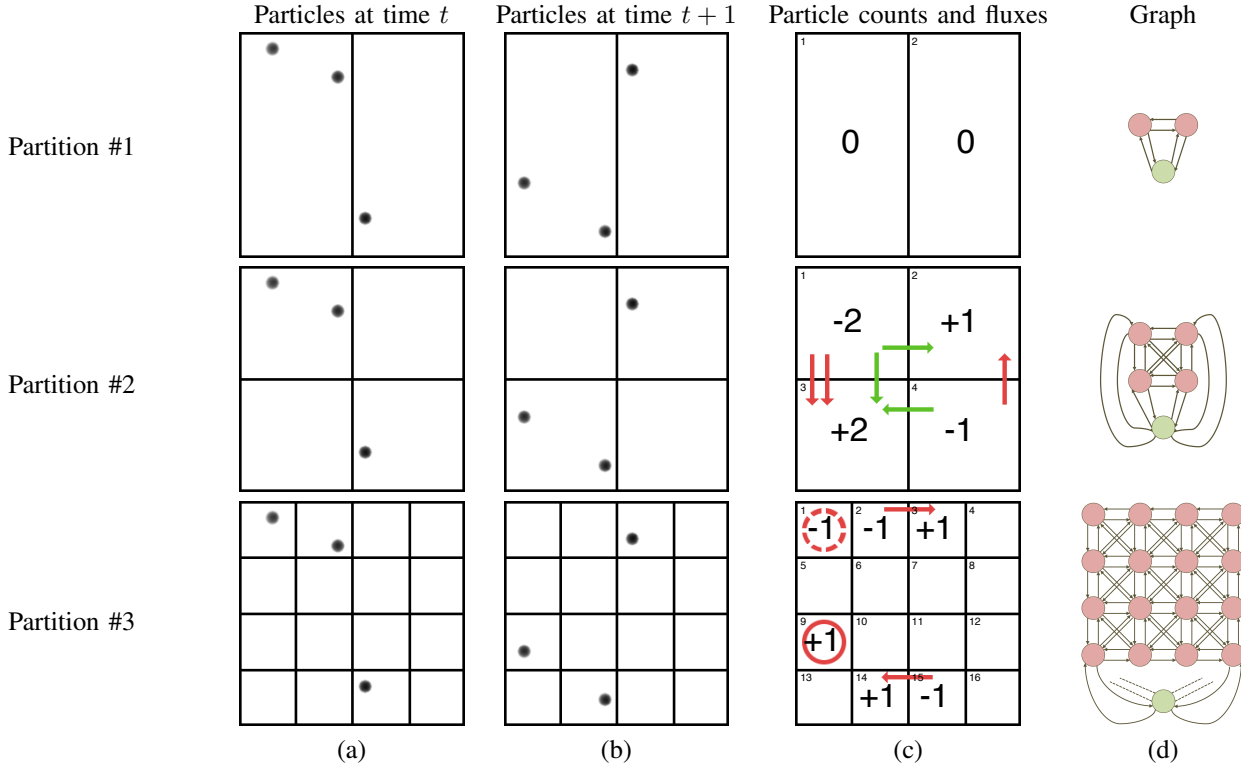


Fig. 2. (a-b) Particle positions at time t (a) and time $t+1$ (b); (c) difference of the number of particles between t and $t+1$ for each region and possible particle fluxes represented as colored arrows (the region numbers are indicated at the top left of every region); (d) graphs associated to the three arbitrary partitions where the virtual region is represented in green.

baseline approach (nearest neighbor correspondence) on artificial image sequences. In Section IV, the interest of the method is demonstrated on 3D real image sequences showing vesicular trafficking within single cells expressing the protein Rab6-GFP. In Section V, we present the advantages and the limitations of the proposed framework and we discuss the relationships with the optical flow and particle tracking approaches. Section VI contains concluding remarks.

Notations: Throughout the paper, the matrices are denoted by bold upper-case letters \mathbf{A} and the vectors by bold lower case letters \mathbf{a} . We denote the i th element of a vector \mathbf{a} by a_i , a set A by upper-case letters and $|A|$ denotes the cardinal of set A . The ℓ_2 norm of vector \mathbf{a} is denoted by $\|\mathbf{a}\|_2 = \sqrt{\sum_i a_i^2}$ and the ℓ_1 norm by $\|\mathbf{a}\|_1 = \sum_i |a_i|$.

II. FLUX ESTIMATION ON AN IMAGE PARTITION

In this section, we first present the concept of flux analysis based on particle counting by using a toy example. We then develop the mathematics for particle and intensity flux estimation and optimization.

A. Proof of concept: a toy example

Let us assume an image domain uniformly partitioned into fixed-size and fixed-shape regions and a set of particles moving over time within this domain. We propose to infer the number of particles moving from one adjacent region to another from the variations of the number of particles in each region

from two consecutive frames. Let us consider three particles observed at each time step as illustrated in Fig. 2 and assume three different image partitions respectively composed of 2, 4 and 16 regions as shown in Fig. 2. For each partition strategy, the variation of the number of particles is indicated in Fig. 2 c).

When considering the partition with 2 regions, the difference of the number of particles is equal to 0 in both regions, suggesting that there are no particles moving across their common boundary. In the case of the partition with 4 regions, assuming no particle appearance and disappearance, two scenarios are possible:

- i) two particles moved from region #1 to region #3 while one particle moved from region #4 to region #2;
- ii) one particle moved from region #1 to region #2, one particle moved from region #1 to region #3 and one particle moved from region #4 to region #3.

Finally, in the case of the partition with 16 regions, only one possible solution exists assuming that the exchanges between adjacent regions are more plausible than the particle appearances and disappearances. Indeed, one particle moved from region #2 to region #3 and one particle moved from region #15 to region #14, one particle disappeared in region #1 and one particle appeared in region #9.

This trivial example allows us to make three comments:

- 1) An approach based on the variation of particle numbers within a given region enables estimating particle movements.

- 2) The number of regions needs to be high enough to disambiguate several competitive scenarios.
- 3) If the particle fluxes between neighboring regions are not favored with respect to particle appearances and disappearances, all the particle fluxes will be considered as appearance or disappearance processes.

These points will be quantitatively studied in Section III. In the next section, we formulate the flux estimation problem as a convex optimization problem.

B. Representation of the flux

In the previous section, we have shown how it is possible to infer the particle motion across the boundaries of an image partition from the variations of the number of these particles over time in each region by assuming that the variations of the particle number over time in each region and by assuming that the total particle number is preserved over time. This idea shares a strong connection with optical flow (see Section I) where usually, a data term reflects the constancy over time of quantities such as brightness or intensity gradients. In the case of the analysis of the movement of particles used as tracers within a fluid [30] or the movement of clouds from satellite imaging [31], the intensity is generally assumed to be related to the density of the observed quantity [32], [33]. Therefore, with some approximations, the image intensity follows the continuity equation in fluid mechanics, which can be written as:

$$\frac{\partial \rho}{\partial t} + \text{div}(\mathbf{f}) = s, \text{ such that } \mathbf{f} = \rho \mathbf{v}, \quad (1)$$

with ρ the mass density, $\mathbf{v} = (v_x, v_y)^\top$ the velocity and s a spatially varying source term. Our aim is to estimate \mathbf{f} through the boundary ∂R separating two regions R . From the divergence theorem, we have $\int_R \text{div}(\mathbf{f}) dV = \int_{\partial R} \mathbf{f} \cdot \mathbf{n} dS$ where \mathbf{n} denotes the surface normal.

In the discrete setting, let us now consider the set of the regions R_i with $i \in [1, |V|]$ defining a partition of the image domain Ω . The associated oriented graph $\mathcal{G}(E, V)$ contains $|E|$ edges and $|V|$ vertices, where E denotes the set of edges associated to boundaries between two adjacent regions and V the set of vertices associated to the regions. Moreover, in order to deal with possible appearances and disappearances of particles (either due to biophysical/biochemical processes or over/under detections), a virtual region is added to the graph and connected to each region of this partition. In what follows, $y_i(t)$ denotes the evolution over time of the number of particles $y_i^P(t) \in \mathbb{Z}^+$ or the intensity level $y_i^I(t) \in \mathbb{R}^+$ in each region $i \in [1, |V|]$ at time $t \in [1, T]$. On this discrete grid, the conservation equation (1) now leads to:

$$\frac{\partial \mathbf{y}(t)}{\partial t} - \mathbf{M}\mathbf{x}(t) = 0, \quad (2)$$

where $\mathbf{y}(t) = (y_1(t), \dots, y_{|V|}(t))^\top$ and $\partial y_i(t)/\partial t \triangleq y_i(t+1) - y_i(t)$. This equation allows us to associate the particle flux vector $\mathbf{x}(t) = (x_1(t), \dots, x_{|E|}(t))^\top$ with the temporal variations $\partial y_i/\partial t$ of particle numbers in each region $i \in [1, |V|]$. In this

modeling, the divergence operator $\mathbf{M} = [m_{ij}]$ is a $|V| \times |E|$ matrix such that for each vertex i and edge j , we have:

$$m_{ij} = \begin{cases} 1 & \text{if edge } j \text{ points to vertex } i, \\ -1 & \text{if edge } j \text{ originates from vertex } i, \\ 0 & \text{otherwise.} \end{cases} \quad (3)$$

If the number of particles in the virtual region i^* is not accessible by definition, it can be estimated from the variation of the total number of particles:

$$z_{i^*}(t) = -\frac{\partial}{\partial t} \sum_{i \in V \setminus i^*} y_i(t). \quad (4)$$

Finally, the full observation vector considering the virtual region $i^* \in V$ is defined as

$$\mathbf{z}(t) = \left(\frac{\partial y_1(t)}{\partial t}, \dots, \frac{\partial y_{|V|-1}(t)}{\partial t}, z_{i^*}(t) \right)^\top \quad (5)$$

and the proposed model can be written as

$$\mathbf{z}(t) - \mathbf{M}\mathbf{x}(t) = 0, \quad t \in [1, T-1], \quad (6)$$

including in its general form the fluxes from and towards the virtual region.

C. Non-negative sparse flux estimation

Instead of assuming a spatial smoothness constraint which would not always be relevant since the size of the region can be large, we propose to seek for a sparse positive solution. The non-negativity is required as we are considering an oriented graph.

The number of edges being higher than the number of vertices, the flux estimation is an ill-posed problem and additional constraints are necessary to find a relevant solution. Note that the appearance of a particle and the disappearance of another particle lead to two particle fluxes, from and towards the virtual region i^* , while a particle that is moving from one region to an adjacent region only involves one single particle flux. Therefore, imposing a sparse constraint favors fluxes between regions and discourages appearances and disappearances.

To be concise, we will drop the variable t and just use \mathbf{x} to denote the flux vector and \mathbf{z} to denote the observation. Formally, the flux estimation problem is formulated as LASSO optimization problem [34]:

$$(\mathbf{P}_1) \quad \min_{\mathbf{x} \geq 0} \frac{1}{2} \|\mathbf{z} - \mathbf{M}\mathbf{x}\|_2^2 + \kappa \|\mathbf{x}\|_1 \quad (7)$$

where the ℓ_1 norm is used as sparsity proxy and κ is a real positive parameter. To solve this non differentiable convex minimization problem, several efficient algorithms have been developed such as the ADMM [35], [36] or PPA [37].

We have further investigated another formulation of the problem (\mathbf{P}_1) as:

$$(\mathbf{P}_2) \quad \min_{\mathbf{x}} \frac{1}{2} \|\mathbf{z} - \mathbf{M}\mathbf{x}\|_2^2 + \kappa \|\mathbf{x}\|_1 + \frac{1}{2} d_C^2(\mathbf{x}), \quad (8)$$

where d_C^2 denotes the squared distance of \mathbf{x} to the space C of the positive solutions, defined in a point-wise fashion as:

$$d_C^2(\mathbf{x}) = \sum_{i=1}^{|E|} d_C^2(x_i), \quad (9)$$

and

$$d_C^2(x_i) = \begin{cases} 0 & \text{if } x_i \geq 0, \\ x_i^2 & \text{otherwise.} \end{cases} \quad (10)$$

This approach allows to include the non-negativity in a “softer” way and lets the algorithm reach the optimal solution with a smooth trajectory in a dozen of iterations. To minimize this 3-term cost function, we consider the PPXA algorithm [37], a multi-term extension of the Douglas-Rachford algorithm [38] relying on the following proximity operators:

$$\text{prox}_{\frac{1}{2}d_C^2}(x_i) = \begin{cases} x_i & \text{if } x_i \geq 0, \\ x_i/2 & \text{otherwise,} \end{cases} \quad (11)$$

applied to each coordinate of the vector \mathbf{x} . The ℓ_1 -norm proximal operator corresponds to the following soft-thresholding:

$$\text{prox}_{\kappa\|\cdot\|_1}(x_i) = \begin{cases} x_i - \kappa & \text{if } x_i \geq \kappa, \\ x_i + \kappa & \text{if } x_i \leq -\kappa, \\ 0 & \text{otherwise,} \end{cases} \quad (12)$$

which is also applied to each coordinate of the vector \mathbf{x} . Finally, the proximity operator associated to the squared ℓ_2 -norm involving the linear operator \mathbf{M} is defined by:

$$\text{prox}_{\frac{1}{2}\|\mathbf{M}\mathbf{x}-\mathbf{z}\|^2}(\mathbf{x}) = (\mathbf{I} + \mathbf{M}\mathbf{M}^\top)^{-1}(\mathbf{x} + \mathbf{M}^\top\mathbf{z}) \quad (13)$$

with \mathbf{I} denoting the identity matrix. The PPXA and ADMM proximal minimization approaches are well suited when the operator \mathbf{M} remains of reasonable size and/or sparse. We have tested both approaches and have obtained the same results in a similar range of time (ADMM being slightly faster when using sparse matrices). When the size of the problem increases, it is possible that the algorithms that do not compute the direct inversion of $\mathbf{M}^\top\mathbf{M}$ such as FISTA [39] will be more suited.

The proposed approach can be applied to both variation of intensity and variation of a discrete number of particles. In the latter case, one may suggest that the problem is now an integer problem and that dedicated algorithms may prove to be more efficient. However, solving integer programs is NP-hard and the proposed approach can be seen as a relaxation technique. Moreover, as the matrix \mathbf{M} is totally unimodular (being a network matrix), it can be proven that the solution converges towards an integer solution (see e.g., [20]).

III. EVALUATION ON SYNTHETIC IMAGE SEQUENCES

In this section, we describe the performance of the proposed approach with respect to the region connectivity, the particle density, velocity and rate of appearances and disappearances. The robustness of the sparsity parameter κ is shown as well.

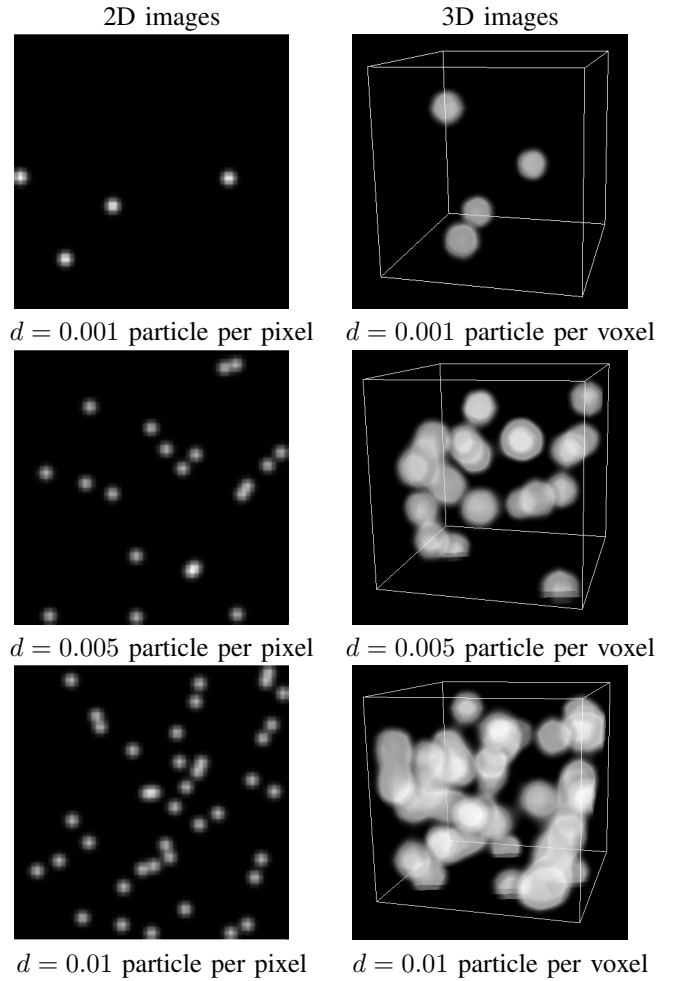


Fig. 3. Examples of images and volumes extracted from sequences simulated with three different particle densities.

A. Simulation settings

We consider synthetic sequences of 50 images or volumes to evaluate the performance of the Particle Flux Estimation (PFE). In these sequences, the particles are moving according to a directed motion along a direction that is changing over time combined with a random walk. The particle velocity is slightly and randomly varying over time around $v_{max} = 3$ pixels or voxels per frame. Image and volume sequences are simulated for three different particle densities as illustrated in Fig. 3: i) $d = 0.001$ pp/pv (particle per pixel/particle per voxel); ii) $d = 0.005$ pp/pv; iii) $d = 0.01$ pp/pv. Note that in this evaluation, the density of particles is higher than those usually considered for particle tracking benchmarks [40]. The particle coordinates are directly used to estimate the particle fluxes and no noise is added to those coordinates. For each simulation, the true positive probability (sensitivity) P_d is defined as the ratio between the number of accurately estimated particle fluxes and the total number of particles that cross a common boundary between two regions over the sequence. The probability of false alarm (specificity) P_{fa} is defined as the ratio between the number of false alarms and the number of actual boundary crossings. For all evaluations, P_d and P_{fa} are averaged over 50 simulations for the same set

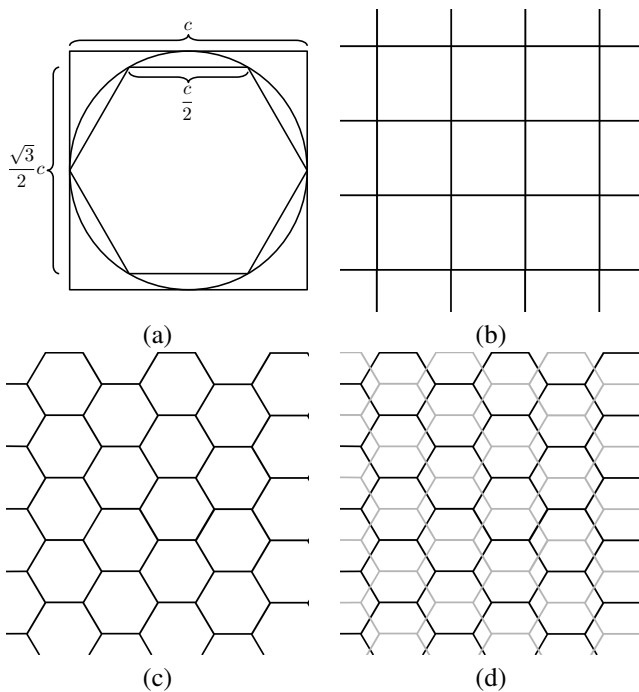


Fig. 4. (a) Correspondence between a square and a hexagon used for squared (b) and hexagonal (c) partitions; (d) superposition of two consecutive hexagonal grids along the z-axis and shifted in the xy plane.

of parameters to take into account the simulation variability.

B. Influence of region size and connectivity

We first apply the PFE on a regular grid of squares (see Fig. 4 (b)) and regular hexagons (see Fig. 4 (c)) on sequences of 64×64 pixel images. The estimation is performed for different square and hexagon sizes. As shown in Fig. 4 (a), the square side length is equal to c while the hexagon side length is equal to $\frac{c}{2}$ and the distance between parallel sides is equal to $\frac{\sqrt{3}}{2}c$. The results shown in Fig. 5 (a) confirm that the smaller the regions are, the better the estimation is, up to a critical region size where the particles can move from one region to another region with no common boundary in the image partition. This critical size is formally obtained when $c = v_{max}$ for squared regions and $\frac{c}{2} = v_{max}$ for hexagonal regions. But most of the time for hexagonal regions, a particle that moves from one region to another that is not adjacent will have to travel the distance between the parallel sides, *i.e.*, $\frac{\sqrt{3}}{2}c$. In that case, the critical size becomes $c = \frac{2}{\sqrt{3}}v_{max}$. In Fig. 5 (a), P_d maximum and P_{fa} minimum are reached when $c = 4$, a value between $\frac{2}{\sqrt{3}}v_{max}$ and $2v_{max}$. Consequently, the lower bound for region size depends on v_{max} . Then, if the performance is increasing up to the critical size when the particle density is high, good results are obtained with larger regions when the particle density is low. Consequently, the upper bound of region size depends on particle density. As shown in Fig. 5 (a), the estimation obtained with the hexagonal partition is more accurate for higher particle densities. For a hexagonal partition, each region has 2 neighbors less than for a squared partition, that means 4 edges less per node. The divergence operator \mathbf{M} is then sparser and the optimization

process is facilitated, leading to an improved estimation. Consequently, hexagonal partitions are preferable to squared partitions.

We then apply the PFE to $16 \times 16 \times 16$ voxel volume sequences by considering two different hexagonal partitions: i) a superposition of hexagons with a thickness equal to $\frac{\sqrt{3}}{2}c$, inducing 20 neighbors per region; ii) a superposition of hexagons with a thickness equal to $\frac{\sqrt{3}}{2}c$ but shifted as shown in Fig. 4 (d), leading to 14 neighbors per region. The results are shown in Fig. 5 (b). From 2D to 3D, the number of neighbors increases from 6 to 14 or 20, that is 16 or 28 more edges for each node than in 2D. The optimization process then becomes more complex and the results are less satisfying. As shown in Fig. 5 (b), the estimation results are more accurate with 14 neighbors than with 20 neighbors. This confirms that regions with the minimum number of neighbors imply the minimum number of edges, leading to a sparser divergence operator and a better performance. Again, the results are improving when the regions are smaller. But differently from the results obtained with 2D images, the performance is still increasing for regions smaller than the critical size, particularly for high particle densities. Presumably, the errors coming from particles moving from one region to another region with no common boundary are compensated by a more efficient estimation obtained with smaller regions, shifting the optimal region size.

From these experiments, we conclude that the optimal region size depends on the particle maximum velocity and particle density. The best performance is reached with an image partition with the minimum number of neighbors.

C. Influence of particle appearance and disappearance rate

To evaluate the impact of particle appearances and disappearances on the PFE, a probability for the particles to appear and disappear at each time step is introduced in the sequences. To measure the global performance of the PFE, we compare this approach with the nearest neighbor matching algorithm (NNMA) that associates each particle at time t to the nearest particle at time $t+1$. The particles that move from one region to a neighboring region contribute to the fluxes estimated with this method. To use this method when the particles appear or disappear, the area or volume considered to look for the nearest neighbor is bounded by the maximum particle velocity. The results obtained for image and volume sequences with a varying particle appearance and disappearance probability are shown in Fig. 6. c is set to 6 for the NNMA to assure that no particle flux is missed. For the PFE, c is set to 3.5 for image sequences with $d = \{0.001, 0.005\}$, to 3 for image sequences with $d = 0.01$, to 3 for volume sequences with $d = 0.001$ and to 2.5 for volume sequences with $d = \{0.005, 0.01\}$. For both 2D and 3D simulations, the NNMA provides a higher P_d than the PFE when no particle appears or disappears. In contrast, the particle appearances and disappearances slightly affect the performance obtained with the PFE while they significantly deteriorate the results obtained with the NNMA. It also has to be noted that the P_{fa} value obtained with the PFE method is always lower than the P_{fa} value obtained with the NNMA. These results demonstrate that the PFE is extremely robust to

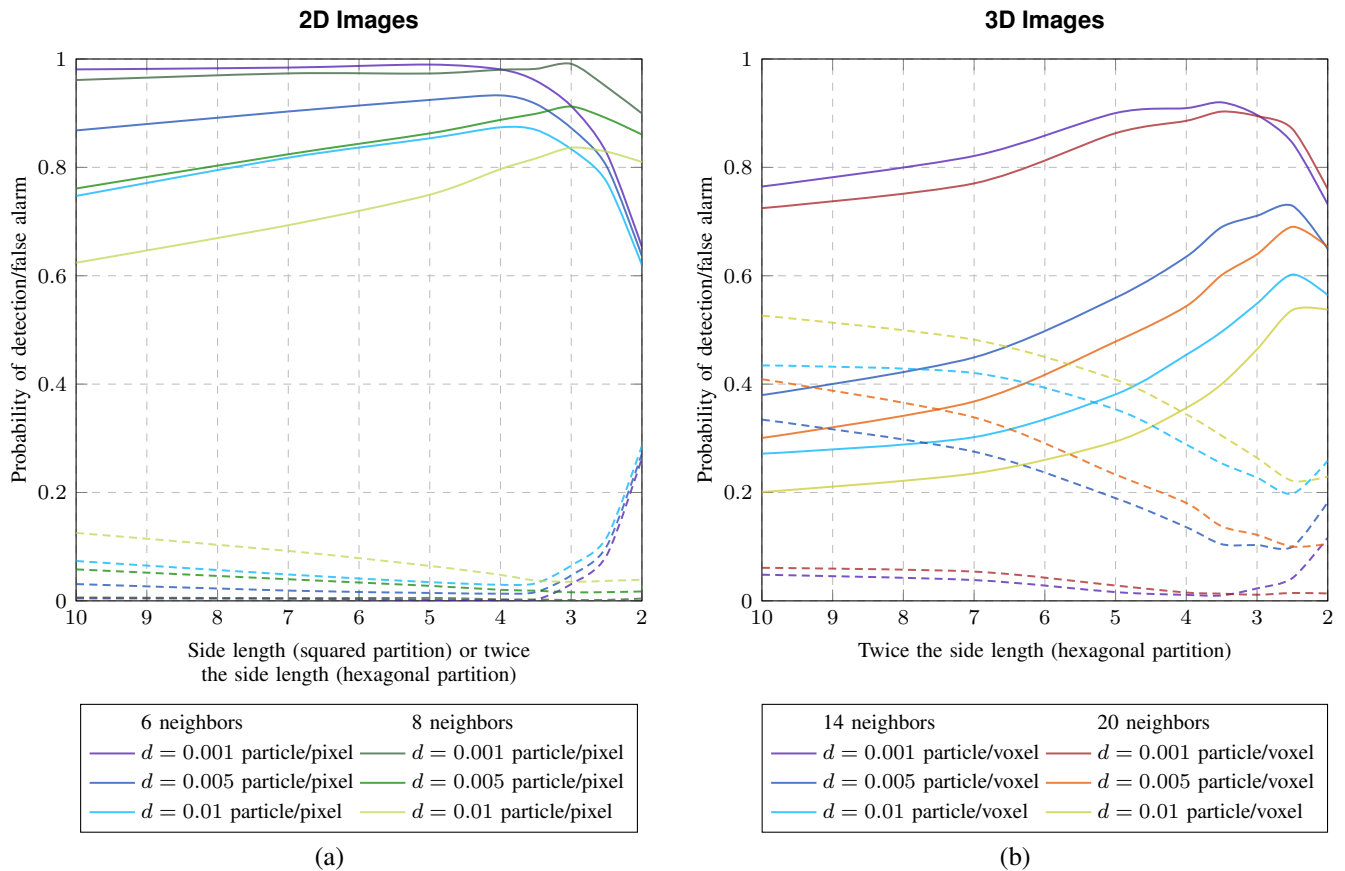


Fig. 5. Results obtained with the particle flux estimation method for squared and hexagonal image partitions with varying region sizes and three different particle densities for 2D and 3D image sequences. The true positive probability P_d , defined as the ratio between the number of accurately estimated particle fluxes and the total number of particles that cross the partition boundaries from frame to frame, is represented as solid lines. The probability of false alarm P_{fa} , defined as the ratio between the number of false alarms and the number of actual boundary crossings, is represented as dashed lines.

particle appearances and disappearances. Consequently, if the detection method used to provide the data to the PFE extracts a high number of false detections, these events are considered as particle appearances and disappearances by the PFE and the particle fluxes between regions are still accurately estimated.

D. Influence of the sparsity parameter κ

Finally, the robustness of the PFE with respect to the parameter κ is evaluated. Simulations with a particle density $d = 0.005$ pp/pv and a probability for the particles to appear and disappear from 0 to 0.5 are generated. The PFE is applied to these simulations for a value of κ that is defined between 0.25 and 3. The results presented in Fig. 7 demonstrate the robustness of the PFE with respect to κ . If κ is large enough ($\kappa > 0.5$), the results are extremely similar. In the following experiments, κ is set to 1.

IV. ANALYSIS OF RAB6 MEMBRANE TRAFFICKING

In this section, we apply the flux estimation method to real 3D data in order to analyze the dynamics of Rab6 positive membranes for crossbow-shaped and disk-shaped cells.

1) *Biological context*: Rab6 are membrane associated proteins attached to moving vesicles from the Golgi apparatus (bright region at the cell center in first and third rows of

Fig. 8) to the cell periphery where it transiently accumulates [41]. In our study, shapes of the cells are constrained with micro-fabricated patterns [42]. Previous studies showed that micro-patterns influence the spatial distribution of cellular endomembranes [43]. But their influence on membrane dynamics has never been explored.

2) *Microscopy*: We used HeLa cells stably transfected with GFP-tagged proteins. A spinning-disk confocal microscope (Ti Eclipse, Nikon, S.A, France) equipped with spinning disk system and a CoolSnap (HQ2 CCD from Roper Scientific S.A.R.L, France) was used to acquire 3D 380 x 380 x 8 stacks (the voxel resolution is 64.5 nm x 64.5 nm x 300 nm) at a rate of one stack per second.

3) *Image processing and analysis*: A variance stabilization [44] is first applied to the 3D stacks as a pre-processing step. The C-CRAFT algorithm [3] is then performed to obtain the object component for each sequence defined at point p and time t as

$$c(p, t) = \begin{cases} I(p, t) & \text{if a particle is detected} \\ 0 & \text{otherwise,} \end{cases}$$

where $I(p, t)$ is the intensity at point p and time t for which the background intensity has been subtracted. Other methods could be applied [9]. The particle centers are defined as the mass centers of the connected components extracted from the

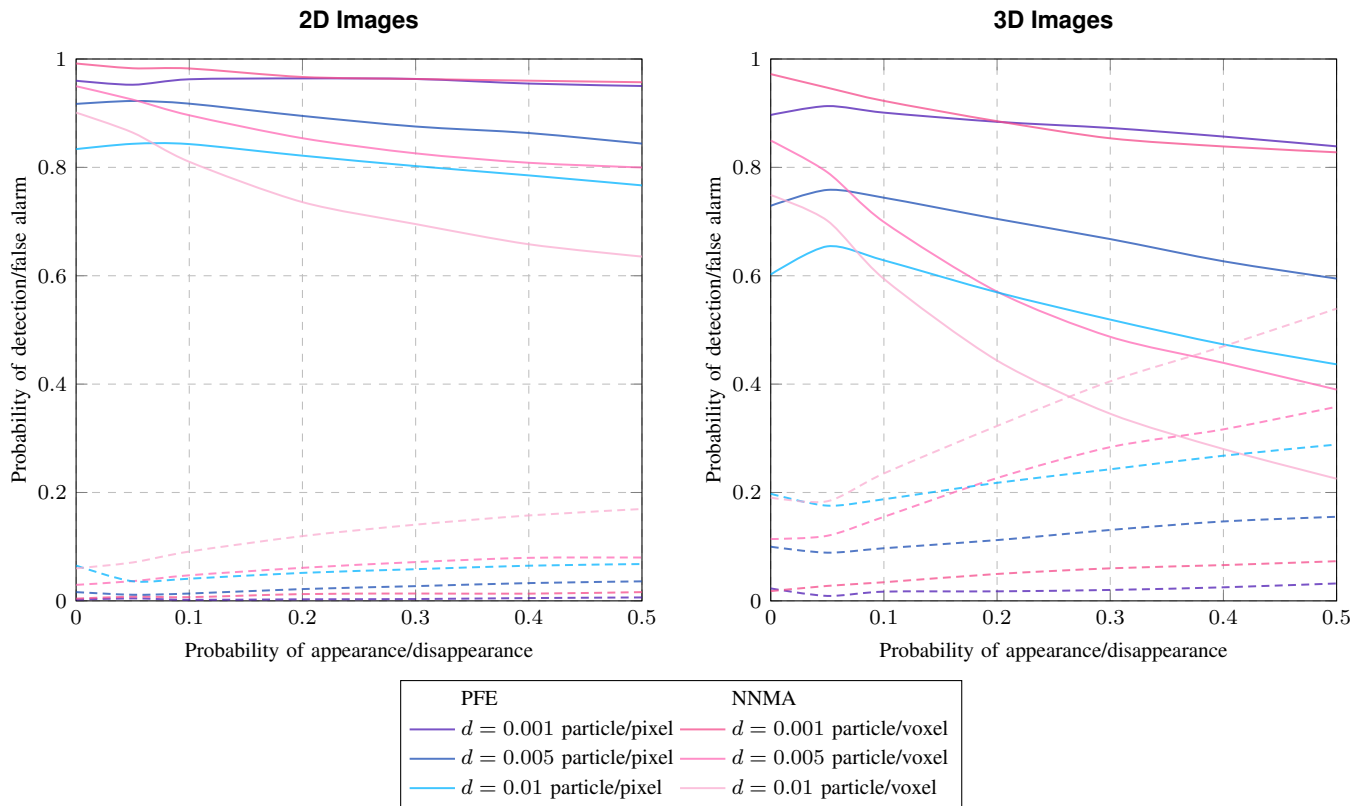


Fig. 6. Results obtained with the particle flux estimation (PFE) method and the nearest neighbor matching algorithm (NNMA) for a varying probability of particle appearances and disappearances and three different particle densities for 2D and 3D image sequences. The true positive probability P_d , defined as the ratio between the number of accurately estimated particle fluxes and the total number of particles that cross the partition boundaries from frame to frame, is represented as solid lines. The probability of false alarm P_{fa} , defined as the ratio between the number of false alarms and the number of actual boundary crossings, is represented as dashed lines.

object component. To compare all sequences, these results are registered together by considering the direction between the Golgi center and the cell center (resp. the crossbow orientation) for the disk-shaped cells (resp. the crossbow-shaped cells). From these registered coordinates, the number of particles in every region of the image partition is computed to define \mathbf{y}^P for particle flux estimation. The average intensity measured over each connected component in the object component is summed over each region of the image partition at each time step to define \mathbf{y}^I for intensity flux estimation:

$$y_i^I(t) = \frac{1}{|\mathbb{1}[c(p, t) > 0]|} \sum_{p \in R_i} c(p, t),$$

where $\mathbb{1}[\cdot]$ denotes the indicator function. As the intensity is proportional to the amount of proteins, it might be more accurate to estimate intensity fluxes than particle fluxes. In these sequences, the particle density is low (about 0.0002 pv). Therefore, we choose a region size that is quite large ($c = 10$). To take into account the resolution anisotropy, the region thickness is equal to $10 \times 64.5/300 = 2.15$. As trafficking is not occurring at the Golgi region and outside the cell, a mask is defined for every sequence accordingly.

4) *Disappearance fluxes*: Previous studies [3], [45] showed that Rab6 trafficking is oriented towards the crossbow tips for crossbow-shaped cells while it is uniform for disk-shaped cells. This distribution suggests that the Rab6 trafficking end-

points are located at the tips of the crossbow for crossbow-shaped cells and are uniformly distributed at the cell periphery for disk-shaped cells. To validate this assumption, we extract the fluxes going to the virtual region that correspond to particle disappearances. The set of the disappearance particle fluxes and disappearance intensity fluxes are first summed over time for each sequence and then averaged over sequences showing crossbow-shaped or disk-shaped cells. These results are shown in Fig. 9. As the studied sequences are noisy, some estimated disappearance fluxes correspond actually to false or missed detections. However, the results confirm the initial assumption: particle end-points are primarily located at the tips of the crossbow for crossbow-shaped cells while they are uniformly located at the cell periphery of the disk-shaped cells. Differences between intensity and particle fluxes are not striking even though the intensity fluxes seem to better highlight the crossbow tips.

5) *Multi-resolution analysis*: To go further in the global dynamics analysis of the Rab6 positive membranes, we propose to analyze the estimated flux at a coarser scale and define a new image partition with larger regions (see Fig. 10). As the region size needs to be small enough to get a good flux estimation (see Section III), we transcribe the estimated fluxes on the partition defined with regions where $c = 10$ on this cruder image partition. For example, in the partition shown in Fig. 10 (a), all the fluxes that originate in the central

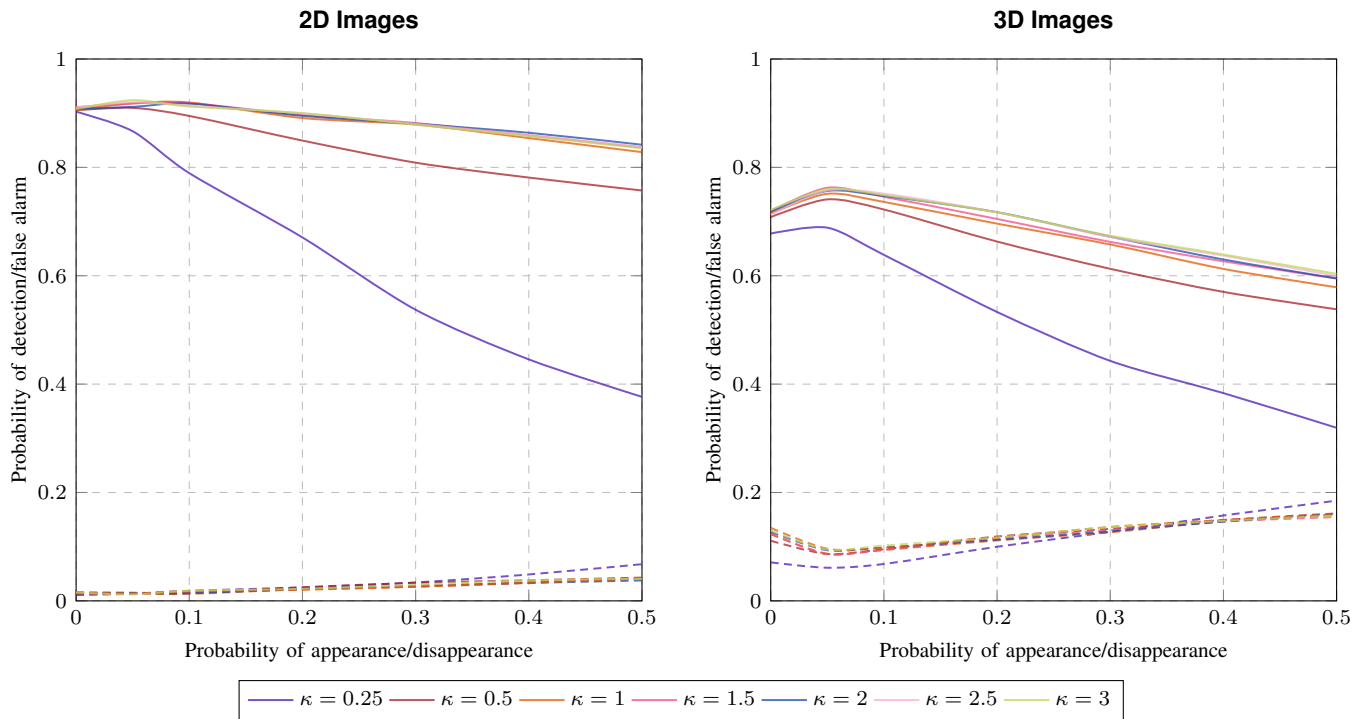


Fig. 7. Results obtained with the particle flux estimation (PFE) method for a varying probability of particle appearances and disappearances, a particle density equal to 0.05 pp/pv and different values for the parameter κ for 2D and 3D image sequences. The true positive probability P_d , defined as the ratio between the number of accurately estimated particle fluxes and the total number of particles that cross the partition boundaries from frame to frame, is represented as solid lines. The probability of false alarm P_{fa} , defined as the ratio between the number of false alarms and the number of actual boundary crossings, is represented as dashed lines.

region and terminate in the next top left region in the partition defined with regions where $c = 10$ are summed to define flux #10. These fluxes are then grouped according to four different categories related to direction: i) fluxes towards the cell periphery (green arrows in cell partitions of Fig. 10); ii) fluxes towards the Golgi (red arrows in Fig. 10); iii) lateral fluxes in the inner crown (purple arrows in Fig. 10); iv) lateral fluxes in the outer crown (blue arrows in Fig. 10). In a previous study [46], the authors tracked individually vesicles associated with Rab6 positive membranes and evaluate the proportion of vesicles heading to the cell periphery (36%), to the Golgi (24%), and moving in a lateral direction (40%) in unconstrained HeLa cells. This study confirmed that the Rab6 positive membranes predominantly move to the cell periphery (as lateral directions are divided into two opposite directions, corresponding to $2 \times 20\%$). In our study, we divide the lateral directions into two different categories to evaluate if the vesicles have the same behavior when they are close to the Golgi or close to the cell periphery. The results are reported in Fig. 11. These results demonstrate that for micro-patterned cells, Rab6 positive membranes are predominantly trafficking towards the cell periphery. This behavior is even more striking for disk-shaped cells. For both micro-patterns, the lateral fluxes in the outer crown are more important than lateral fluxes in the inner crown, especially for crossbow-shaped cells. This indicates that Rab6 trafficking is more directed in regions close to the Golgi than in regions located at the cell periphery. This might be due to the vesicle docking step that is happening before vesicle reach their end-point,

corresponding to a random walk close to the end-point. Finally, the estimated particle and intensity fluxes are extremely close, indicating that intensity is quite uniformly distributed over the particles.

V. DISCUSSION

In this section, we first present how to define an image partition before applying the flux estimation. We then compare the flux estimation with optical flow and particle tracking methods. Finally, we compare particle and intensity flux estimations based on particle counting and mean intensity measurements.

A. Setting of algorithm parameters

As shown in Sections III-B and III-C, the flux estimation accuracy depends on the partition topology and region size, the particle density and the probability of particle appearances and disappearances. The region size has to be small enough to alleviate critical cases. The higher the particle density is, the smaller the region size needs to be, up to the critical size when the particles can move from one region to another region that are not neighbors. The partition topology greatly impacts the results as it can complexify the optimization procedure. Consequently, it is important to choose an image partition that minimizes the number of neighbors for each region. It has to be noted that the particle appearances and disappearances slightly impact the flux estimation. As demonstrated in Section III-D, the flux estimation is very robust to the parameter κ and a value superior to 0.5 leads to similar results.

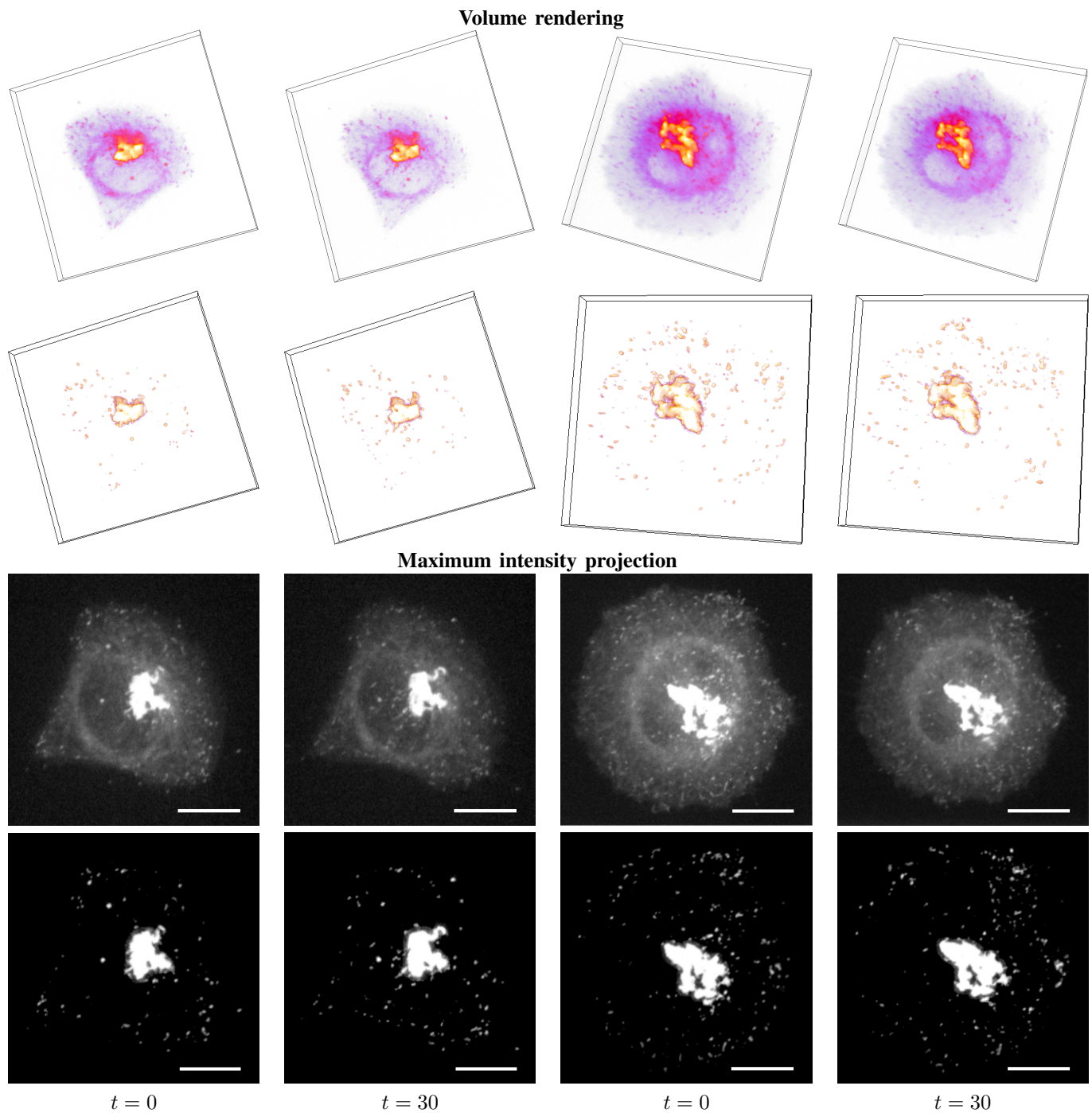


Fig. 8. First two rows: volume rendering of fluorescent images (first row) and the corresponding object component obtained with [3] (second row) taken from two sequences showing Rab6 proteins in a crossbow-shaped (left) or a disk-shaped (right) cell; last two rows: maximum projection along the z-axis of the same images shown in the two first rows. The scale bars correspond to $5 \mu\text{m}$.

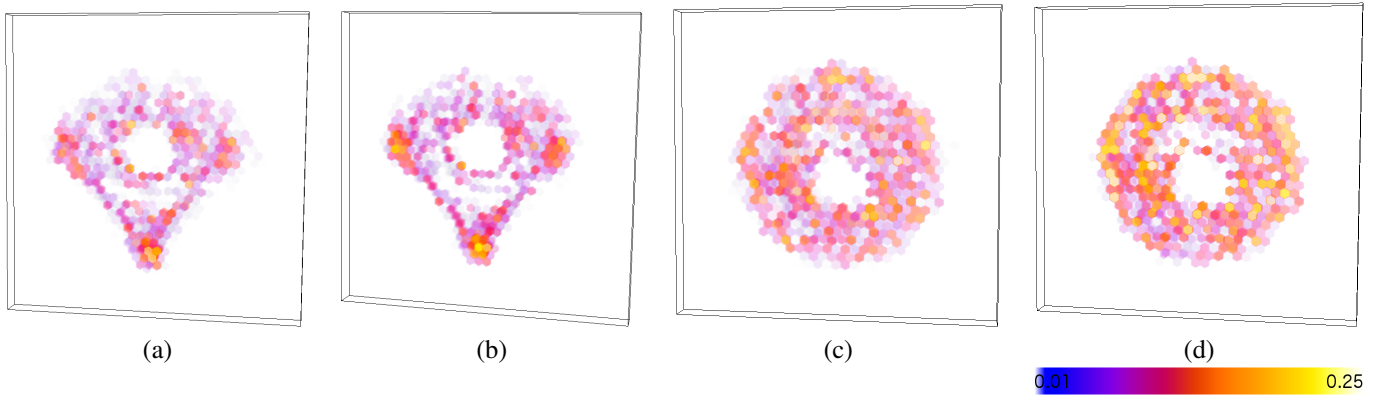


Fig. 9. Volume rendering of the disappearance particle (a;c) and intensity (b;d) fluxes averaged over 15 sequences with crossbow-shaped cells (a-b) or 15 sequences with disk-shaped cells (c-d). The color code defines the disappearance rate represented in the volume renderings.

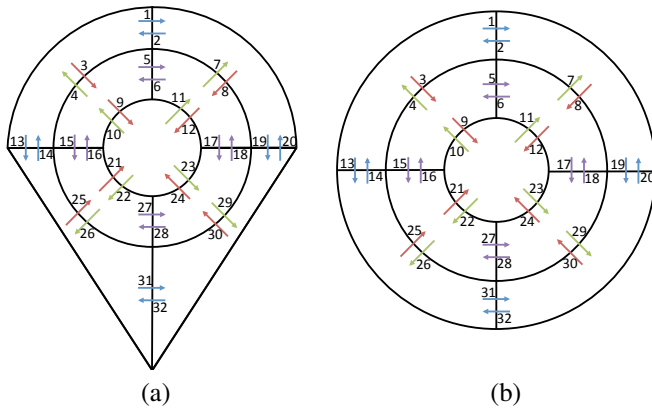


Fig. 10. Cell partition of a crossbow-shaped cell (a) and a disk-shaped cell (b). The edge identification numbers are written next to each edge. Green edges are oriented towards the cell periphery, red edges are oriented towards the Golgi, purple edges correspond to lateral fluxes in the inner crown and blue edges to lateral fluxes in the outer crown.

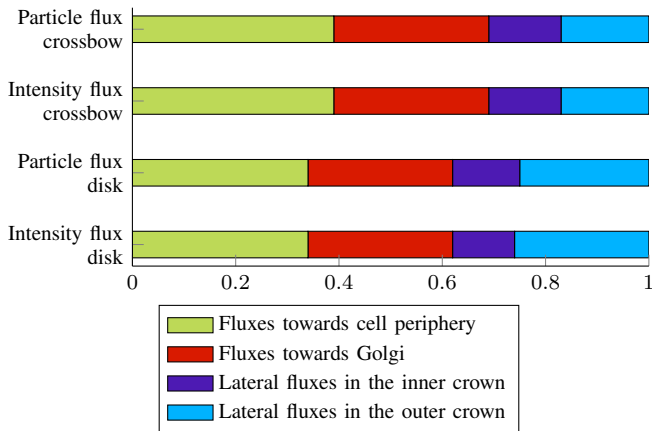


Fig. 11. Particle and intensity fluxes estimated for cell partitions shown in Fig. 10 over all sequences and grouped according to four different categories.

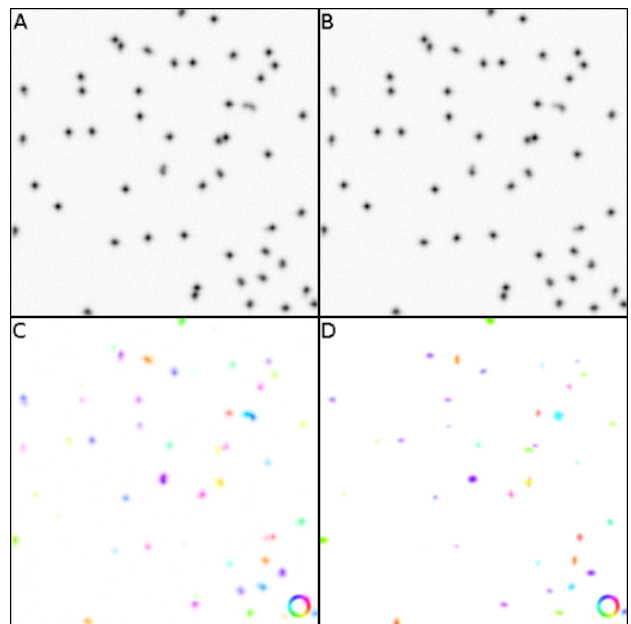


Fig. 12. Comparison with optical flow on a synthetic data set. The first frames A and B represent the original data composed of 50 particles moving randomly with a velocity of 1 pixel per frame. In C, the flux estimate given by the product of the intensity with a local optical flow estimator [24] is represented with a color-coding of the vector field and in D, the flux estimated with the PFE is displayed.

In future works, we will investigate in details the trade-off between particle density, region size and optimization to be able to define the optimal image partition for a given problem.

B. Pixel-wise flux estimation

When the regions tend to the pixel size, the flux estimation modeling is close to the optical flow framework. To illustrate this idea, we do not represent the graph of regions by a matrix M but rather represent the operator M by the divergence operator $-\text{div}$. In this context, we use the FISTA algorithm [39] which does not involve the inversion of $M^T M$ but only requires the computation of the gradient of the cost function and the projection associated to the ℓ_1 constraint. We compare this pixel-wise flux estimation with the product of the intensity

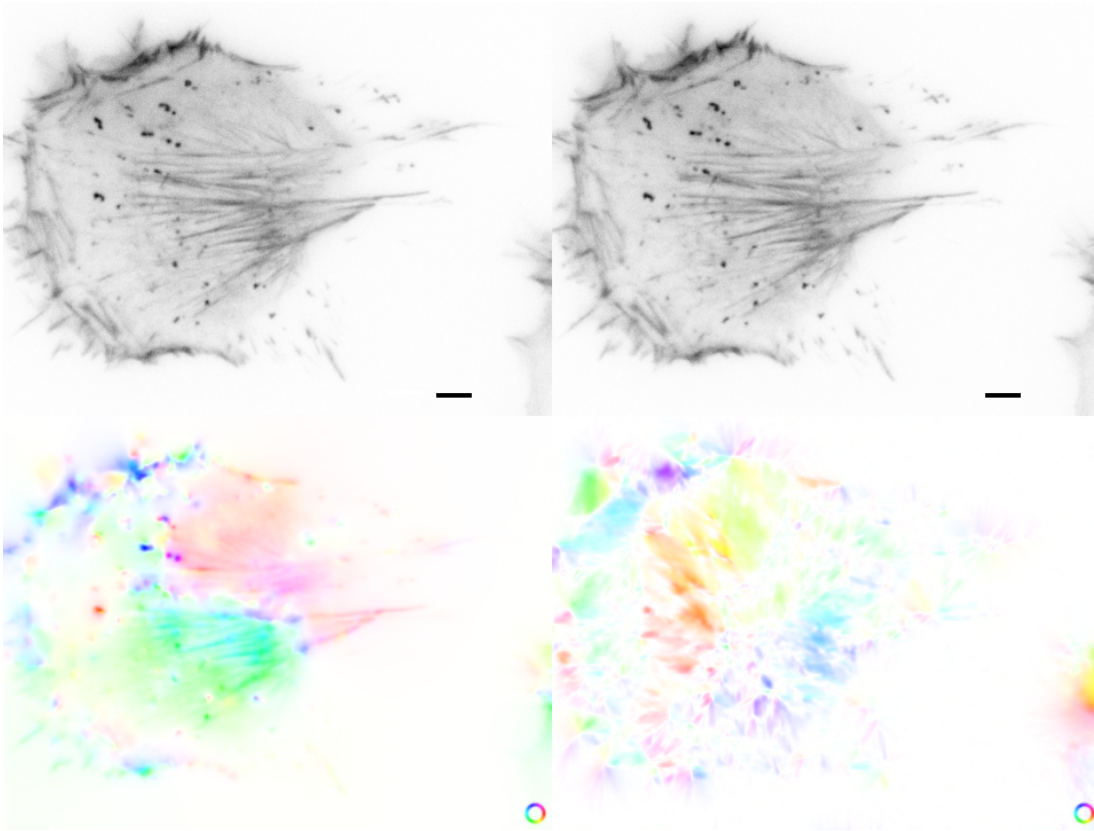


Fig. 13. Comparison with optical flow on an image pair. These images depict a RPE1 cell expressing LifeAct acquired using total internal reflection microscopy (TIRF). The cell is progressing towards the left with a contraction movement. The scale bars correspond to $5 \mu\text{m}$. In the lower panels, the fluxes estimated by a standard multi-scale Horn and Schunck algorithm [47] (lower left) and the proposed method (lower right) are displayed as color coded according to their orientations. The movement is well captured by the proposed method while the flux estimated from the product of the intensity and the optical flow seems unrelated to the actual displacement (large green and red regions).

considered as the local density ρ and the motion vector field v estimated with an optical flow method.

In a first experiment, we use a synthetic dataset representing 50 particles randomly moving and displayed in Fig. 12. We can see that the PFE method (shown on the right) allows to recover the motion of these moving particles as much as a Lucas and Kanade motion estimator [24]. In a second experiment displayed on Fig. 13, we have applied the proposed approach to a real dataset representing a RPE1 cell expressing LifeAct that is moving from the right to the left. These images were acquired with total internal reflection microscopy (TIRF). This experiment shows that the proposed method is able to capture a different information than the flux computed with the global optical flow method [47]. Visually, the fluxes from the right to the left displayed in red on the right part of the cell and the fluxes from the upper left to the right displayed in blue correspond well to the contraction of the cell.

C. Optical flow computation versus flux estimation

Optical flow methods aim at estimating velocity vector fields while the flux estimation approach leads to particle fluxes and fluorescence intensity fluxes between neighbor regions. By considering particle counts and intensity measurements, the flux estimation modeling manages to estimate discrete fluxes over time, a task that optical flow methods generally fail to

achieve. The flux estimation also allows a sparse modeling of the fluxes that is not addressed in optical flow methods.

D. Particle tracking versus flux estimation

The flux estimation approach aims at quantifying fluxes between predefined adjacent regions from two consecutive frames. Similar traffic features could be obtained from tracks given pairs of regions. In our framework, the flux estimation method provides a global optimum and is very robust to particle appearances and disappearances. Only two free parameters are tuned by the user: i) the region size that depends on particle density and velocity; ii) a robust parameter that controls the sparsity of traffic modeling. Additionally, this method exploits particle counts and image intensity information to estimate fluxes and can be applied to sequences with high particle densities. Finally, the flux estimation allows a sparse modeling of the fluxes that is not addressed in particle tracking methods.

E. Particle flux versus intensity flux

In Section IV, we estimate both particle and intensity fluxes on real 3D image sequences. In our experiment, the two estimation methods produced similar results. The intensity-based approach could be applied without object detection and segmentation by measuring the intensity difference in each

region of the partition between two consecutive time steps. This would be particularly well adapted to situations with no background. Note that the fluorescence intensity is known to be proportional to protein concentration and can potentially be more appropriate for a large variety of applications.

VI. CONCLUSION

In this paper, we have presented an original approach for monitoring intracellular activity by retrieving fluxes between adjacent regions from particle countings and mean intensity measurements. We have developed an estimation procedure with a sparsity constraint on the fluxes. We have evaluated this approach with respect to the particle density, velocity, appearance and disappearance rate, the region size and the sparsity parameter values. We have finally demonstrated the interest of the method for the quantification of Rab6 positive membrane trafficking. This approach can be used to get low-level traffic features given by fluxes between small regions or for high-level analysis given an appropriate partition of the cell. For testing purpose, we provide an online version of our implementation: <http://mobyte-serpico.rennes.inria.fr/cgi-bin/portal.py#forms::FLUX>.

In this study, unidirectional fluxes were defined to compare the approach with methods such as the nearest neighbor matching algorithm. We plan to consider bidirectional fluxes to reduce the number of vertices and consequently the dimensionality of the divergence operator \mathbf{M} in order to simplify the optimization problem. We also intend to look at super pixel-based image representation [48] to improve the flux estimation model and to adapt better to structures in the cell.

VII. ACKNOWLEDGMENTS

The authors acknowledge France-BioImaging infrastructure supported by the French National Research Agency (ANR-10-INBS-04-07, "Investments for the future").

REFERENCES

- [1] J. Boulanger, A. Gidon, C. Kervrann, and J. Salamero, "A patch-based method for repetitive and transient event detection in fluorescence imaging," *PLoS ONE*, vol. 5, no. 10, p. e13190, 2010.
- [2] A. Gidon, S. Bardin, J. Boulanger, F. Waharte, B. Cinquin, L. Heliot, H. de la Salle, D. Hanau, C. Kervrann, B. Goud, and J. Salamero, "Dynamics of Rab11a-MyoVb-FIP2 complex frames the late recycling steps of langerin from the ERC to the plasma membrane," *Traffic*, vol. 13, pp. 815–833, 2012.
- [3] T. Pécot, P. Bouthemy, J. Boulanger, A. Chessel, S. Bardin, J. Salamero, and C. Kervrann, "Background fluorescence estimation and vesicle segmentation in live cell imaging with conditional random fields," *IEEE Trans. Image Proc.*, vol. 4, no. 2, pp. 667–680, 2015.
- [4] T. Pécot, J. Boulanger, C. Kervrann, P. Bouthemy, and J. Salamero, "Estimation of the flow of particles within a partition of the image domain in fluorescence video-microscopy," in *Proc. IEEE Int. Symp. Biomed. Imaging*, Beijing, China, 2014, pp. 453–456.
- [5] Y. Vardi, "Network tomography: Estimating source-destination traffic intensities from link data," *J. American Stat. Ass.*, vol. 91, no. 433, pp. 365–377, 1996.
- [6] J. Boyd, J. Meloche, and Y. Vardi, "Statistical tracking in video traffic surveillance," in *Proc. IEEE Int. Conf. Comput. Vision*, vol. 1, Corfu, Greece, 1999, pp. 163–168 vol.1.
- [7] T. Pécot, C. Kervrann, and P. Bouthemy, "Minimal paths and probabilistic models for origin-destination traffic estimation in live cell imaging," in *Proc. IEEE Int. Symp. Biomed. Imaging (ISBI)*, Paris, France, 2008, pp. 843–846.
- [8] S. Mukherjee, N. Ray, and S. T. Acton, "Counting cells from microscopy videos without tracking individual cells," in *Proc. IEEE Int. Symp. Biomed. Imaging (ISBI)*, Beijing, China, 2014, pp. 465–468.
- [9] I. Smal, M. Loog, W. Niessen, and E. Meijering, "Quantitative comparison of spot detection methods in fluorescence microscopy," *IEEE Trans. Med. Imaging*, vol. 29, no. 2, pp. 282–301, 2010.
- [10] Y. Kalaidzidis, "Intracellular objects tracking," *Eur. J. Cell Biol.*, vol. 86, no. 9, pp. 569–578, 2007.
- [11] M. F. Kircher, S. S. Gambhir, and J. Grimm, "Noninvasive cell-tracking methods," *Nat. Rev. Clin. Oncol.*, vol. 8, no. 11, pp. 677–688, 2011.
- [12] I. Sbalzarini and P. Koumoutsakos, "Feature point tracking and trajectory analysis for video imaging in cell biology," *J. Struct. Biol.*, vol. 151, no. 2, pp. 182–195, 2005.
- [13] G. Yang, A. Matov, and G. Danuser, "Reliable tracking of large scale dense antiparallel particle motion for fluorescence live cell imaging," in *Proc. Comp. Vision Patt. Recog.-Workshops (CVPR)*, San Diego, USA, 2005, pp. 138–138.
- [14] W. J. Godinez and K. Rohr, "Tracking multiple particles in fluorescence time-lapse microscopy images via probabilistic data association," *IEEE Trans. Med. Imaging*, vol. 34, no. 2, pp. 415–432, 2015.
- [15] K. Jaqaman, D. Loerke, M. Mettlen, H. Kuwata, S. Grinstein, S. Schmid, and G. Danuser, "Robust single-particle tracking in live-cell time-lapse sequences," *Nature Methods*, vol. 5, pp. 695–702, 2008.
- [16] D. Delibaltov, S. Karthikeyan, V. Jagadeesh, and B. Manjunath, "Robust biological image sequence analysis using graph based approaches," in *Proc. IEEE Sig. Syst. Comp. (ASILOMAR)*, Pacific Grove, USA, 2012, pp. 1588–1592.
- [17] I. Smal, E. Meijering, K. Draegestein, N. Galjart, I. Grigoriev, A. Akhmanova, M. E. van Royen, A. B. Houtsmuller, and N. Niessen, "Multiple object tracking in molecular bioimaging by Rao-Blackwellized marginal particle filtering," *Med. Image Anal.*, vol. 12, no. 6, pp. 764–777, 2008.
- [18] N. Chenouard, I. Bloch, and J.-C. Olivo-Marin, "Multiple hypothesis tracking for cluttered biological image sequences," *IEEE Trans. Patt. Anal. Mach. Intell.*, vol. 35, no. 11, pp. 2736–2750, 2013.
- [19] L. Liang, H. Shen, P. De Camilli, and J. S. Duncan, "A novel multiple hypothesis based particle tracking method for clathrin mediated endocytosis analysis using fluorescence microscopy," *IEEE Trans. Image Proc.*, vol. 23, no. 4, pp. 1844–1857, 2014.
- [20] J. Berclaz, F. Fleuret, E. Turetken, and P. Fua, "Multiple objects tracking using K-shortest paths optimization," *Patt. Anal. Mach. Intell.*, vol. 33, no. 9, pp. 1806–1819, 2011.
- [21] L. Ji and G. Danuser, "Tracking quasi-stationary flow of weak fluorescent signals by adaptive multi-frame correlation," *J. Microsc.*, vol. 220, no. 3, pp. 150–167, 2005.
- [22] K. Rohr, W. J. Godinez, N. Harder, S. Worz, J. Mattes, W. Tvarusko, and R. Eils, "Tracking and quantitative analysis of dynamic movements of cells and particles," *Cold Spring Harb. Protoc.*, vol. 2010, no. 6, 2010.
- [23] D. L. Kolin and P. W. Wiseman, "Advances in image correlation spectroscopy: measuring number densities, aggregation states, and dynamics of fluorescently labeled macromolecules in cells," *Cell Biochem. Biophys.*, vol. 49, no. 3, pp. 141–164, 2007.
- [24] B. D. Lucas and T. Kanade, "An Iterative Image Registration Technique with an Application to Stereo Vision," in *Proc. Int. Joint Conf. Artificial Intell.*, San Francisco, USA, 1981, pp. 674–679.
- [25] I. H. Kim, Y. C. Chen, D. L. Spector, R. Eils, and K. Rohr, "Nonrigid registration of 2-D and 3-D dynamic cell nuclei images for improved classification of subcellular particle motion," *IEEE Trans. Image Process.*, vol. 20, no. 4, pp. 1011–1022, 2011.
- [26] M. Pinot, V. Steiner, B. Dehapiot, B. K. Yoo, F. Chesnel, L. Blanchoin, C. Kervrann, and Z. Gueroui, "Confinement induces actin flow in a meiotic cytoplasm," *Proc. Natl. Acad. Sci. U.S.A.*, vol. 109, no. 29, pp. 11 705–11 710, 2012.
- [27] L. Pizarro, J. Delpiano, P. Aljabar, J. Ruiz-del Solar, and D. Rueckert, "Towards dense motion estimation in light and electron microscopy," in *IEEE Proc. Int. Symp. Biomed. Imaging (ISBI)*, Chicago, USA, 2011, pp. 1939–1942.
- [28] J. Delpiano, J. Jara, J. Scheer, O. A. Ramírez, J. Ruiz-del Solar, and S. Härtel, "Performance of optical flow techniques for motion analysis of fluorescent point signals in confocal microscopy," *Mach. Vis. App.*, vol. 23, no. 4, pp. 675–689, 2012.
- [29] T. Lecomte, R. Thibaux, N. Guillen, A. C. Dufour, and J.-C. Olivo-Marin, "Fluid optical flow for forces and pressure field estimation in cellular biology," in *IEEE Proc. Int. Conf. Image Proc. (ICIP)*, Orlando, USA, 2012, pp. 69–72.
- [30] R. J. Adrian, "Particle-Imaging Techniques for Experimental Fluid Mechanics," *Annual Rev. Fluid Mech.*, vol. 23, no. 1, pp. 261–304, 1991.

- [31] T. Corpetti, E. Memin, and P. Perez, "Dense estimation of fluid flows," *IEEE Transactions on Pattern Analysis and Machine Intelligence*, vol. 24, no. 3, pp. 365–380, 2002.
- [32] J. M. Fitzpatrick, "The existence of geometrical density-image transformations corresponding to object motion," *Comput. Vision, Graph., Image Proc.*, vol. 44, no. 2, pp. 155–174, 1988.
- [33] S. Ozeré, P. Boutheymy, F. Spindler, P. Paul-Gilloteaux, and C. Kervrann, "Robust parametric stabilization of moving cells with intensity correction in light microscopy image sequences," in *Proc. IEEE Int. Symp. Biomed. Imaging (ISBI)*. IEEE, 2013, pp. 468–471.
- [34] R. Tibshirani, "Regression Shrinkage and Selection via the Lasso," *J. Royal Stat. Soc.*, vol. 58, no. 1, pp. 267–288, 1996.
- [35] D. Gabay and B. Mercier, "A dual algorithm for the solution of nonlinear variational problems via finite element approximation," *Comput. Math. App.*, vol. 2, no. 1, pp. 17–40, 1976.
- [36] S. Boyd, N. Parikh, E. Chu, B. Peleato, and J. Eckstein, "Distributed Optimization and Statistical Learning via the Alternating Direction Method of Multipliers," *Found. Trends Mach. Learning*, vol. 3, no. 1, pp. 1–122, 2011.
- [37] P. L. Combettes and J.-C. Pesquet, *Fixed-Point Algorithms for Inverse Problems in Science and Engineering*. Springer, New York, 2011, ch. 10. Proximal splitting methods in signal processing, pp. 185–212.
- [38] J. Douglas and H. H. Rachford, "On the numerical solution of heat conduction problems in two and three space variables," *Trans. Am. Math. Soc.*, pp. 421–439, 1956.
- [39] A. Beck and M. Teboulle, "A Fast Iterative Shrinkage-Thresholding Algorithm for Linear Inverse Problems," *SIAM J. Imaging Sc.*, vol. 2, no. 1, pp. 183–202, 2009.
- [40] N. Chenouard *et al.*, "Objective comparison of particle tracking methods," *Nat. Meth.*, vol. 11, pp. 281–289, 2014.
- [41] J. White, L. Johannes, F. Mallar, A. Girod, G. Stephan, S. Reinsh, P. Keller, B. Tzschaschel, A. Echard, B. Goud, and E. Stelzer, "Rab6 coordinates a novel golgi to ER retrograde transport pathway in live cells," *J. Cell Biol.*, vol. 147, no. 4, pp. 743–760, 1999.
- [42] M. Thery, V. Racine, A. Pepin, M. Piel, Y. Chen, J.-B. Sibarita, and M. Bornens, "The extracellular matrix guides the orientation of the cell division axis," *Nat. Cell Biol.*, vol. 7, pp. 947–953, 2005.
- [43] K. Schauer, T. Duong, K. Bleakley, S. Bardin, M. Bornens, and B. Goud, "Probabilistic density maps to study global endomembrane organization," *Nature Meth.*, vol. 7, no. 7, pp. 560–566, 2010.
- [44] J. Boulanger, C. Kervrann, P. Boutheymy, P. Elbau, J.-B. Sibarita, and J. Salamero, "Patch-based non-local functional for denoising fluorescence microscopy image sequences," *IEEE Trans. Med. Imaging*, vol. 29, no. 2, pp. 442–454, 2010.
- [45] K. Schauer, T. Duong, C. Gomes-Santos, and B. Goud, "Studying intracellular trafficking pathways with probabilistic density maps," *Meth. Cell Biol.*, vol. 118, pp. 325–343, 2013.
- [46] V. Racine, M. Saschse, J. Salamero, V. Fraissier, A. Trubuil, and J.-B. Sibarita, "Visualization and quantification of vesicle trafficking on a 3D cytoskeleton network in living cells," *J. Microsc.*, pp. 214–228, 2007.
- [47] B. K. Horn and B. G. Schunck, "Determining optical flow," *Artificial Intell.*, vol. 17, pp. 185–203, 1981.
- [48] R. Achanta, K. Shaji, A. an Smith, A. Lucchi, P. Fua, and S. Susstrunk, "Slic superpixels compared to state-of-the-art superpixel methods," *IEEE Trans. Patt. Anal. Mach. Intell.*, vol. 34, pp. 2274–2282, 2012.



Thierry Pécot graduated from École Nationale d'Ingénieurs de Brest in 2005, received the M.Sc. degree in image analysis and statistics in 2006 and the Ph.D degree in signal analysis and telecommunications in 2010 from the University of Rennes 1, France. From April 2010 to June 2013, he was a post-doctoral fellow with the James Cancer Center at Ohio State University, Columbus, Ohio. Since September 2013, he has joined the Serpico group at Inria research centre in Rennes as a post-doctoral researcher. His main research interests are related to

intracellular trafficking analysis, fluorescence microscopy, motion estimation, segmentation and dynamics modeling in cell biology.



Charles Kervrann received the M.Sc. degree in 1992 and the Ph.D degree in 1995 in Signal Processing and Telecommunications from the University of Rennes 1, France. He obtained his HDR (Habilitation thesis) in Signal Processing and Telecommunications from the University of Rennes 1 in 2010. From 1997 to 2010, he was researcher at the INRA Applied Mathematics and Informatics Département (1997–2003, Jouy-en-Josas, France) and he joined the VISTA Inria research group in 2003 (Rennes, France). In 2010, he was appointed to the rank of Research Director 2nd class Inria (DR2), Inria Research Centre in Rennes. His is currently the head of the Serpico research group. His current research interests include mathematical and statistical methods for biological image processing and microscopy. His work focuses on image sequence denoising, motion estimation, object detection, noise modeling for microscopy, traffic and dynamics modeling in cell biology. He has served as member of the program committees of the major conferences in image processing and computer vision.



Jean Salamero obtained the Ph.D degree in Immunology at the University Paris VI in 1985, in the laboratory INSERM U253. His thesis work focused on autoimmune diseases, experimentally induced in mice. During post-doctoral internships at EMBL (Heidelberg) and at UCSHC (Denver, Colorado) in the team of Dr. Kathryn Howell (Cell Biology Departments), he reconstituted the generation of vesicles from purified Golgi membranes, in a cell free assay. It was during this post-doctoral period (1986–1988) that he became familiar with the biochemical

and morphological techniques of modern cell biology. Having obtained a research position at CNRS, he joined the newly formed team of Jean Davoust (CIML, Marseille) in 1989 in Marseille. From then until now, he became interested in biophysics, microscopy and bio-imaging. Since 1995 he is at the UMR 144 CNRS-Institut Curie, where his main biological topic is the study of membrane trafficking in diverse cellular systems. He is heading the team Space-time imaging of cellular dynamics of organelles and endomembranes and the Cell and Tissue Imaging Core Facility at the Institut Curie (Pict-IBiSA).



Jérôme Boulanger graduated in 2003 from École Nationale Supérieure de Physique, Marseille and received in 2007 the Ph.D degree in Signal Processing and Telecommunication from the University of Rennes 1, France. From 2007 to 2008, he was with the Institut Curie in Paris and till 2010 with the Radon Institut from Applied Mathematics in Linz, Austria. In 2011, he joined the CNRS at Institut Curie in Paris. His research is focused on image processing for microscopy image analysis.